INFORMATICS JOURNALS

*Critical Minerals Metals and Materials*
eISSN: xxxx-xxxx; DOI: 10.18311/c3m/2026/56221
*Volume 1, Issue 2, June 2026, pp. 00-00*

# Microstructural and Thermal Behavior of Zn-Rich Byproducts from the Iron and Steel Industry

**Khedkar Vinayak Jivanrao*, Shaikh Mahaboob Basha, Munukutla Sri Sai Ramesh, Srinivas Dwarapudi and Atanu Ranjan Pal**

*Agglomeration Research Group, R&D Department, Tata Steel Ltd., Jamshedpur - 831001, Jharkhand, India; vinayak.khedkar@tatasteel.com*

## Abstract

*In an integrated steel plant, byproducts such as blast furnace sludge, steelmaking sludge, and flue dust are reused for agglomeration processes including sinter and pellet production. However, these materials exhibit diverse chemical compositions, particularly high zinc concentrations which limit their utilization. This study investigates the dilatometric and morphological characterization at elevated temperature for selected byproduct samples from an integrated plant. Particle size analysis showed a mean diameter exceeding 100 µm, with 90% passing 500 µm size. Phase analysis revealed the presence of hematite, magnetite, wustite, quartz, and zincite. Microscopy further validated irregular morphologies and zinc distribution. Dilatometry indicated sintering temperatures and melting behaviors ranging from 1000°C to 1500°C, alongside volumetric and area changes. Bulk TGA experiments up to 1300 °C showed continuous mass loss carbon combustion and CO-induced reduction of iron oxides, enabling near-complete zinc volatilization. Post-roasting XRD confirmed reduction pathways and zinc removal in carbon-rich samples. This study highlights characterization, morphology, thermal behavior, high temperature zinc phase behavior and phase transformations as well as the suitability of byproducts in agglomeration processes.*

***Major Findings:*** *Zn-rich steel plant byproducts exhibited distinct particle morphology, phase assemblage, and thermal deformation behavior. Bulk TGA and XRD analyses confirmed near-complete zinc volatilization in carbon-rich samples at 1300 °C. Integrated characterization established the suitability of byproducts for agglomeration processes.*

**Keywords:** *Agglomeration, BF Dust, Dilatometry, Zinc Byproducts, Morphology, Sludge*

## 1.0 Introduction

The integrated steelmaking process involves several key stages: raw material preparation (pellet making, sinter making, and coke making), iron production through the Blast Furnace (BF), and steel production via the Linz-Donawitz (LD) route. Throughout these stages, various wastes and byproducts are generated, which include BF slag, flue dust and sludge, LD slag, LD sludge, LD dust, and mill scale etc. Given that global crude steel production is currently of the order of 1.8–1.9 billion tonnes per year, the associated generation of slags, dusts and sludges represents an enormous material flow, making the management of these streams a critical issue for resource efficiency and environmental protection[1-3]. The generation of waste and byproducts typically amounts to several hundred kg per ton of steel produced. An approximate breakdown of byproduct quantities from the steelmaking process is displayed in Table 1.

*Author for correspondence

**Table 1.** Byproducts in iron and steel industry

| Byproduct name | Quantity generated in kg/ ton of hot metal |
|---|---|
| BF slag | 300-540[4,5] |
| BF flue dust and Sludge | 35-40[6] |
| Steel slag | 100-200[7] |
| LD sludge | 10-30[8,9] |
| Mill scale | 22-30[10,11] |
| Mill Sludge | 12-15[12] |

These byproducts contain valuable resources such as iron, carbon, calcium, and FeO, alongside undesirable gangue materials like zinc, sodium, potassium, and lead[13]. Revert materials can be recycled in processes such as pellet and sinter making. Studies have demonstrated the successful reuse of byproducts like BF flue dust, mill scale, and Gas Cleaning Plant sludge (GCP) to enhance iron content and improve the utilization of these materials in iron ore agglomeration processes[8,14,15].

GCP sludge and flue dust are generated during the BF gas cleaning process and contain significant amounts of valuable components, including total iron in the range of 20–35 % and carbon around 20–35%[16]. LD sludge, on the other hand, contains more iron and calcium oxide[17]. However, these sludges and dust also contain considerable amounts of zinc, in the form of ferrites or oxides, ranging from 0.5% to 7.0%, which poses challenges in their reuse and recycling processes[18]. Consequently, these Zn-bearing fine byproducts are increasingly regarded not merely as wastes but as secondary raw materials whose effective recycling is essential to reduce landfill, recover iron and carbon units, and support circular-economy goals in the steel sector.

Several studies have investigated the utilization of steelmaking byproducts in iron and steel production. Pal et al. developed a binder-less method for producing iron oxide waste micro-pellets using $CO_2$ treatment from LD sludge and BF flue dust, achieving sufficient mechanical strength for sintering[19]. Sharanappa *et al.,* compared the use of different slags in sinter making and found that optimal hot metal desulphurization station slag addition improved sinter properties more than LD slag, validated through plant trials[20]. Arnab *et al.,* explored a direct reduced iron process using iron wastes from sinter plants, BF, and steel melting shops, achieving greater than 91% waste reduction and above 85% metallization in laboratory trials[8]. The potential of mill scale as an additive in iron ore pelletization was examined by Mogale and Umadevi. Both studies found that up to 10% mill scale addition improved pellet properties, with higher concentrations proving detrimental due to increased FeO and cracking. Mogale *et al.,* further explored mill scale's potential as a reductant[10,21]. Sintering process can be enhanced by addition of micro pellets from revert materials[22]. These studies demonstrate the potential for sustainable iron and steel production through the effective recycling of steelmaking byproducts.

The reuse and recycling of revert materials in iron and steel making containing metals such as zinc, alkalis, and lead leads to the progressive accumulation of these elements within the system, especially in BF. This issue is further aggravated by using zinc-rich scrap steel in steelmaking, which introduces additional zinc into the system. As a result, the continuous cycle of concentration leads to elevated levels of zinc and other heavy metals in both iron and steel production, negatively affecting production efficiency and product quality[18,23,24]. Zinc compounds negatively impact BF lining life due to their cyclical behavior between high and low temperature zones within the furnace. Zinc enters the furnace primarily through raw materials and gradually accumulates in the lining, causing degradation of refractory. Consequently, reducing zinc input and managing its cyclical behavior within the furnace are crucial for extending lining lifespan[25]. Residual zinc oxides in metallized pellets, used as a recycling product, can lead to significant vaporization and condensation in steel making process. This causes accumulation of zinc in off-gas pipelines, resulting in clogging and potential erosion of refractory linings. Furthermore, zinc's high volatility can lead to zinc emissions, posing environmental concerns[26]. From a circular-economy perspective, it is therefore necessary to characterise the behaviour of Zn-rich byproducts

at high temperature, identify operating windows where iron units can be safely recycled, and route the volatilised zinc to dedicated recovery processes so that both iron and zinc value streams are captured rather than discarded.

Previous studies have investigated the utilization of individual steelmaking by-products in agglomeration and reduction processes; however, most works focus on optimizing recycling routes or zinc removal pathways in isolation. Limited attention has been given to integrated characterization that correlates particle size, morphology, phase assemblage, and high-temperature volumetric behavior with recyclability constraints imposed by zinc-bearing phases along with the Bulk Thermogravimetric Analysis (TGA). In this context, the present study aims to support sustainable metallurgy by systematically characterizing zinc-rich by-products generated in an integrated steel plant. Emphasis is placed on understanding their microstructural features, phase distribution, thermal deformation behavior, and zinc deportment during high-temperature treatment.

### 1.1 Objectives of the Study

- To quantify the chemical composition and particle size distribution of five industrial Zn-bearing byproducts from an integrated steel plant.
- To characterize their microstructure and phase assemblage via SEM–EDS and XRD.
- To evaluate their high-temperature thermal behavior using optical dilatometry and bulk mass loss and Zn volatilization behavior using bulk TGA.
- To assess, based on these measurements and literature benchmarks, their suitability for recycling through agglomeration processes.

## 2. Materials and Methods

### 2.1 Raw Material Characterization

Five byproduct samples were collected from different unit operations of an integrated steel plant (Tata Steel Ltd., Jamshedpur). Samples comprised two dust samples from BF dust catcher plants (samples 1 and 2), LD sludge from the steelmaking shop (sample 3), and two sludge samples from two different BF GCP (samples 4 and 5). The chemical composition of all five samples is compiled in Table 2, determined via X-Ray Fluorescence (XRF) spectroscopy estimated using ThermoFisher Scientific, ARL 9900 series instrument. Samples 4 and 5 have higher zinc contents. All the samples have carbon greater than 22%, except sample 3, which contains highest total iron. Loss on Ignition (LOI) was determined by heating samples to 1000°C in a Nabertherm muffle furnace, measuring the weight loss attributed to the removal of hydrous chemically bonded moisture, volatile matter, and carbon.

**Table 2.** Chemical composition of samples

| Chemical Composition in weight % | Sample 1 | Sample 2 | Sample 3 | Sample 4 | Sample 5 |
|---|---|---|---|---|---|
| Total Fe | 30.20 | 28.13 | 49.00 | 21.27 | 20.83 |
| FeO | 12.26 | 0.00 | 0.00 | 4.52 | 0.00 |
| CaO | 5.86 | 5.21 | 13.38 | 3.49 | 3.81 |
| $SiO_2$ | 16.86 | 17.96 | 4.39 | 17.27 | 9.55 |
| MgO | 3.14 | 2.70 | 5.70 | 2.90 | 2.86 |
| $Al_2O_3$ | 3.46 | 3.21 | 0.54 | 3.39 | 3.23 |
| LOI | 27.86 | 28.88 | 3.43 | 42.11 | 43.26 |
| C | 22.80 | 24.50 | 2.18 | 31.00 | 32.10 |
| ZnO | 0.14 | 0.59 | 0.64 | 6.12 | 7.03 |

The Particle Size Distribution (PSD) was done using Malvern PANalytical Mastersizer 3000+ model via laser diffraction technique. X-Ray Diffraction (XRD) analysis was employed to characterize the crystalline structure and phase composition of the samples. Diffraction patterns were obtained using PANalytical Empyrean Model-X'Pert PRO instrument with a Cu target with Cu-Kα radiation source, operating at 40 kV and 45 mA. The scan was performed over a range of 10-90° with a step size of 0.02°/s. Phase identification was performed by comparing the obtained diffractograms with standard reference patterns from the International Centre for Diffraction Data (ICDD) PDF-2 database using Xpert-Highscore software. To observe the microstructure, powder samples were prepared, and analysis was conducted using Scanning Electron Microscopy (SEM) coupled with Energy Dispersive X-ray Spectroscopy (EDS) machine by Hitachi model flexSEM 1000-II.

To observe the volumetric changes and melting properties of samples with respect to the temperature variation, a dilatometry test was done. Dilatometry is a thermal analysis technique used to measure the change in dimensions of a material as a function of temperature. Samples were prepared by making a briquette of the material with size 3 mm diameter and 3 mm height. Then the samples were heated up to 1600°C at a controlled rate of 10°C/min and cooled in air. Sample projection area and lengths were precisely measured. The measurement was automatically performed by machine software, which compared the sample measurements data against calibrated reference sample. Then a dilatometry curve was plotted, depicting thermal expansion or contraction behavior of the material with respect to temperature. DIN 51730:2007 standard was used to record the deformation, hemisphere and flow temperatures.

## 2.2 Bulk Thermogravimetric Analysis Experiment

The flow sheet of pellet preparation from byproducts for the Bulk TGA studies is illustrated in Figure 1. To facilitate efficient heat dissipation, pellets were prepared from the powder samples listed in Table 2, using a laboratory-scale disc pelletizer (3 kg capacity, 45° inclination, 25 rpm). The powder samples were initially oven dried then ball-milled, followed by the addition of a small quantity of bentonite binder and mixing in a 10 kg capacity Eirich mixer. The resulting pellets, 8–16 mm in diameter, 100 gram in sample weight, were subsequently heat-treated in a Bulk TGA furnace. Analysis was carried out at the laboratory to observe

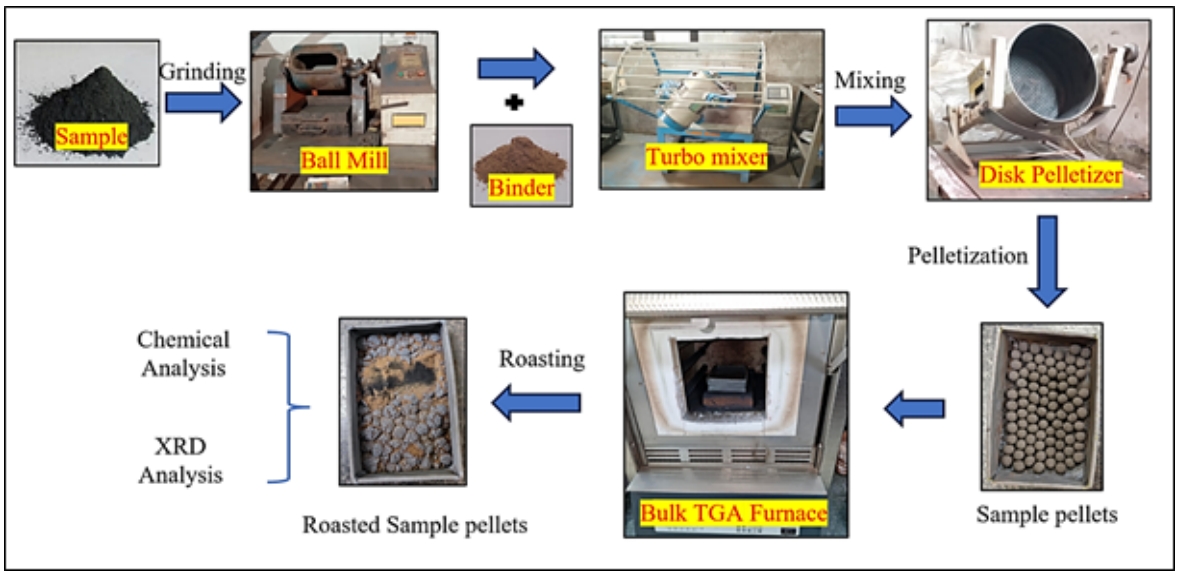


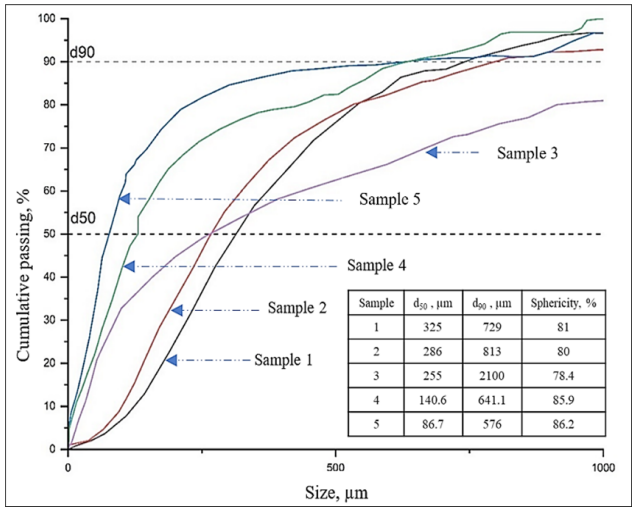

**Figure 1.** Experimental procedure with temperature profile.

the mass change with respect to the temperature. The sample was heated in a rapid heating Nabertherm made muffle furnace in presence of air. The furnace is attached with weighing balance at bottom of sample holder for measuring the weight loss at each second with respect to increasing temperature. Heat treated samples were tested for XRD and chemical analysis.

# 3. Results

## 3.1 Particle Size Distribution

Figure 2 illustrates the cumulative PSD of the raw samples. 50% cumulative passing, or mean size is denoted by $d_{50}$ while $d_{90}$ is 90% cumulative passing size. Sample 5 had the finest PSD whereas sample 1 had the coarsest mean size. Sample 3 depicted the broadest size distribution, with a notably large $d_{90}$ value. Across all samples, particles in samples 4 and 5 exhibited the highest degree sphericity as well as narrower PSD.




| Sample | $d_{50}$ , µm | $d_{90}$ , µm | Sphericity, % |
|---|---|---|---|
| 1 | 325 | 729 | 81 |
| 2 | 286 | 813 | 80 |
| 3 | 255 | 2100 | 78.4 |
| 4 | 140.6 | 641.1 | 85.9 |
| 5 | 86.7 | 576 | 86.2 |

**Figure 2.** Particle size distribution of samples with $d_{50}$, $d_{90}$ and sphericity values.

## 3.2 XRD Analysis of Raw Samples

All samples were crystalline heterogeneous materials. From the XRD analysis, Figure 3 illustrates those dominant phases in sample 1 includes wustite, magnetite, silica, and hematite which. Similarly, Sample 2, 4 and 5 shows reflections corresponding to hematite and silica phases with substantial presence. In samples 4 and 5, Zinc is present mostly in zincite phase. There might be possibility that zinc was present in zinc ferrite form, but the samples 4 and 5 collected were already treated at high reducing conditions, where the zinc ferrite phase reduces to zinc oxide or zinc vapors at temperature above 950°C and reported in BF sludge[27]. Sample 3 has dominant peaks of calcite, wustite and metallic iron while slightly broader peaks of magnetite. While quartz and magnesioferrite phases depicted minor presence.

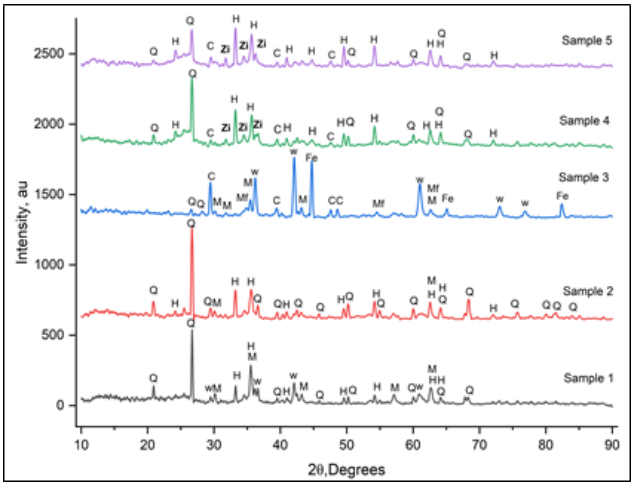



**Figure 3.** Raw materials XRD graph. H: Hematite ($Fe_2O_3$), M: Magnetite ($Fe_3O_4$), W: Wustite (FeO), Q: Quartz ($SiO_2$), Mf: Magnesioferrite ($MgFe_2O_4$), C: Calcite ($CaCO_3$), Zi: Zincite (ZnO).

## 3.3 SEM-EDS Microstructural Analysis

SEM micrographs depicting the morphologies of the samples at 500x magnification are shown in Figure 4. Elemental composition at selected spots, obtained using EDS, are tabulated in Table 3. It is evident from Figures 4-a and b, that in samples 1 and 2, the carbon particles appeared black greyish in color, with coarser, compact lamellar to blocky granular morphology with rounded corners and smooth folded surfaces typical of coke. Such carbonaceous fragments usually originate from mechanical abrasion and fragmentation of coke due to burden descent and gas flow[28,29]. While iron oxides, lime, and gangue particles were finer in size with granular morphology dispersed throughout

the matrix. Typically for pelletization process, raw materials below 150 μm size are used for green balling[30]. The particle shape and size greatly impact the pelletization and sintering processes. Coarser skeletal particles and finer quasi spherical grains from sample 1 and 2 with some surface roughness and porosity can help green pelletization[31,32]. While sintering benefits from irregular to sub-granular fines particles[33].

**Table 3.** EDS elemental composition in weight percentage of SEM micrographs

| | Figure 4-(a) | | | | Figure 4-(b) | | | | Figure 4-(c) | | | | Figure 4-(d) | | | | Figure 4-(e) | | | |
|---|---|---|---|---|---|---|---|---|---|---|---|---|---|---|---|---|---|---|---|---|
| Elements | Spot 1 | Spot 2 | Spot 3 | Spot 4 | Spot 1 | Spot 2 | Spot 3 | Spot 4 | Spot 1 | Spot 2 | Spot 3 | Spot 4 | Spot 1 | Spot 2 | Spot 3 | Spot 4 | Spot 1 | Spot 2 | Spot 3 | Spot 4 |
| C | 35.72 | 69.26 | 19.02 | 52.29 | 72.02 | 63.64 | 58.86 | 12.64 | 5.11 | 9.34 | 7.38 | 5.68 | 85.09 | 27.43 | 60.86 | 14.63 | 15.98 | 66.69 | 29.52 | 64.90 |
| O | 39.91 | 2.35 | 53.37 | 20.38 | 1.78 | 6.61 | 13.3 | 58.21 | 43.47 | 49.76 | 42.91 | 45.70 | 5.18 | 25.6 | 19.78 | 32.85 | 45.15 | 7.94 | 34.43 | 13.74 |
| Mg | 0.31 | 0.25 | 0.77 | 0.37 | 0.21 | 0.17 | 0.22 | 0.30 | 4.19 | 3.42 | 3.12 | 4.63 | 0.26 | 0.83 | 0.23 | 0.81 | 0.41 | 0.21 | 0.59 | 0.52 |
| Al | 1.59 | 0.65 | 2.11 | 0.21 | 0.26 | 1.28 | 0.39 | 0.53 | 0.86 | 0.47 | 0.45 | 0.54 | 0.86 | 5.21 | 1.55 | 3.53 | 3.15 | 0.44 | 1.58 | 1.30 |
| Si | 1.00 | 0.72 | 3.02 | 0.74 | 0.24 | 1.77 | 0.45 | 11.46 | 1.79 | 1.61 | 1.16 | 1.17 | 1.56 | 7.55 | 2.49 | 4.83 | 2.31 | 0.47 | 2.33 | 1.77 |
| Ca | 13.78 | 26.24 | 10.93 | 22.00 | 25.00 | 25.72 | 22.41 | 11.83 | 6.37 | 8.37 | 7.49 | 8.08 | 1.05 | 1.21 | 1.03 | 0.93 | 4.73 | 21.36 | 8.72 | 11.62 |
| Fe | 7.38 | 0.34 | 9.55 | 3.83 | 0.27 | 0.58 | 3.92 | 4.44 | 36.74 | 25.68 | 35.92 | 32.42 | 2.53 | 2.53 | 3.79 | 2.48 | 14.72 | 0.78 | 5.10 | 1.76 |
| Zn | 0.31 | 0.19 | 1.23 | 0.18 | 0.22 | 0.24 | 0.45 | 0.59 | 1.48 | 1.36 | 1.57 | 1.78 | 3.47 | 29.65 | 10.27 | 39.95 | 13.54 | 2.12 | 17.71 | 4.38 |

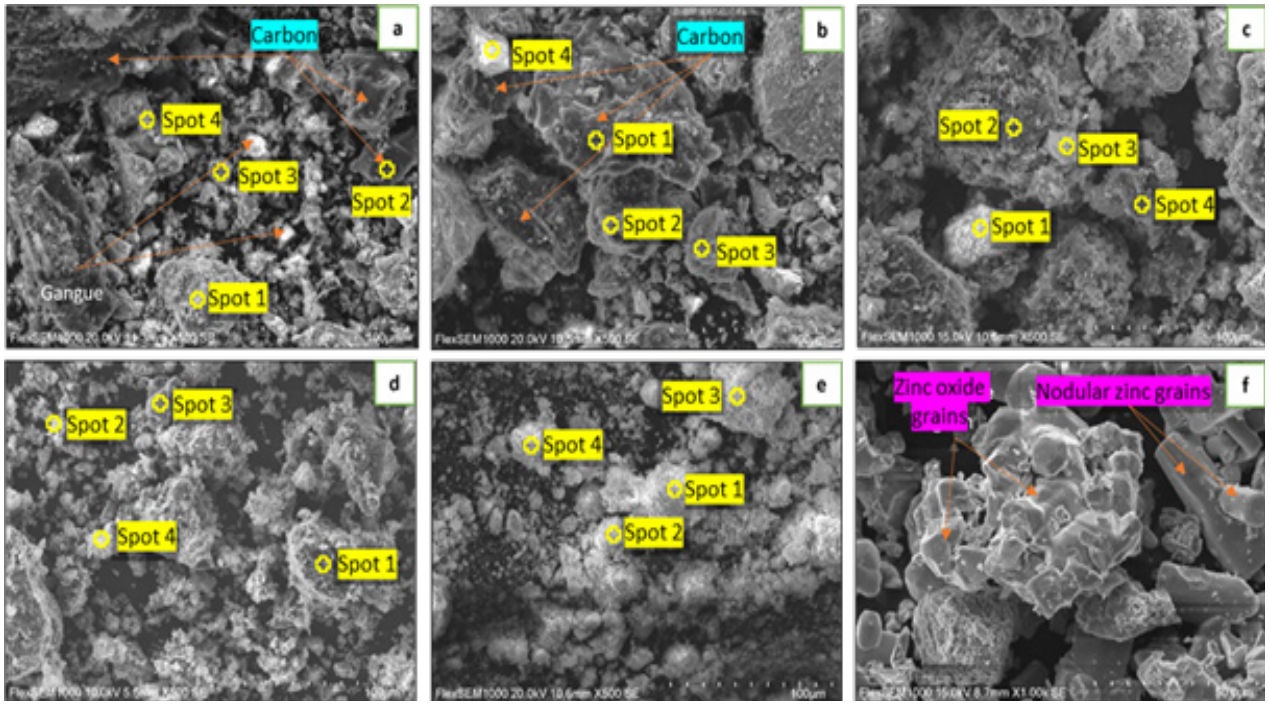



**Figure 4.** SEM micrographs, **(a)**-sample 1, **(b)**-sample 2, **(c)**-sample 3, **(d)**-sample 4, **(e)**-sample 5, **(f)**-Zinc oxide particle.

Hence, samples 1 and 2 with described morphology, considerable carbonaceous fraction are suitable to utilize in sintering process while the finer fraction can be used in pelletizing process.

Illustrated from Figure 4-c, sample 3 displayed a porous morphology, composed of iron oxide particles. The field was dominated by roughly equiaxed, lumpy aggregates with irregular but overall rounded outlines, indicating granulated loose flocs rather than single crystals. Each granule shows highly textured, micro-porous surface made of fused sub-micron particles, suggesting a high internal porosity. These particles result from the presence of lower iron oxides from slag foaming during steelmaking process, coated with dust particles[34]. Wider particle distribution, rough surface texture, and calcite content contributed to the cohesive slimy nature. Highly open loose particles and wide size distribution can hinder the green balling in pelletization, similarly due to cohesive nature, porous clusters can exacerbate sticking and channeling in sinter bed. However, dewatering, homogenization, and micro-pelletizing of material will improve the usability of sample 3[22,35].

The micrograph of sample 4, as shown in Figure 4-d, depicts fluffy aggregates of ultrafine particles. The clusters look lighter rather than compact granules. There were many fine protrusions of iron oxides, gangue material and fine zinc oxide dust as confirmed from spot EDS analysis presented in Table 3, forming filamentous bridges between carbon aggregates. Excess micro-fines and fluffy sludge sharply lower bed permeability in sinter making[36]. While fluffy morphology causes very high-water demand and poor ballability[31,32]. The displayed micrograph of sample 5 in Figure 4-e shows numerous nearly spherical to ellipsoidal granules appeared as dense beads. The background contained very fine particles and small clusters. Zinc phases primarily observed as surface rich coating or very fine inclusions on iron oxides or carbon particles rather coarse crystals leading to their wide dispersal in samples 4 and 5. In samples 1, 2 and 3 only trace amounts of zinc were observed. Mentioned EDS spot values in Table 3, chemical analysis in Table 2, and XRD phase analysis in Figure 3, confirmed the presence of zincite phase in the samples 4 and 5. Presence of rounded granules in sample 5 can improve ballability and can help nucleation in green balling while spherical granules can contribute as fuel reactive fines in sintering process. However, the excess zinc leads to revaporization in sinter beds and recondensation in gas systems, hence utilization should be restricted to limited use or should be diverted to zinc recovery routes[34,37].

## 3.4 Dilatometry

Figure 5 presents the dilatometry results. The graph of percentage area changes versus temperature is shown in Figure 6. The curve reveals information about phase transitions like sintering, melting or crystallization. The term hemisphere temperature is the temperature at which the sample briquette height is half its base width, indicating softening and melting. The flow temperature is reached when the height of briquette is one-third of the base width, signifying complete melting. Figure 5 gives information about melting behavior of samples mentioned as hemisphere and flow temperatures. Sample 3 has the highest flow temperature due to presence of metallic iron and lower amount of gangue. Flow temperatures of samples in descending order were sample 3 > sample 4 > sample 5 > sample 1 > sample 2. The point at which there is sudden decrease in area is noted as sintering temperature where sintering is initiated.

It is evident from Figure 6 that for samples 1 and 2, the substantial area change commenced at 1121°C and 1089°C respectively where the sintering was initiated. While sample 5 exhibited a significant area change at beginning and sintering was initiated at 784°C and sample 4 shows a similar change initiated at a slightly lower temperature of 856°C. The temperatures mentioned gave an idea about burning of carbon particles in the samples. The behavior of sample 3 was intriguing, initially the area increased to 115.5% from 586°C to 1030°C and then rapidly decreased from 1030°C. This suggests phase transformations in sample 3, described in the XRD analysis after roasting, which might have led to area increase. Finer size, amorphous nature of calcite and presence of oxides (iron oxides

| Sample Name | Initial Temperature | Hemisphere Temperature | Flow Temperature | Sintering Temperature |
|---|---|---|---|---|
| Sample 1 |  26°C |  1422°C |  1479°C | 1121°C |
| Sample 2 |  26°C |  1403°C |  1421°C | 1089°C |
| Sample 3 |  26°C |  1405°C |  1510°C | 1030°C |
| Sample 4 |  28°C |  1471°C |  1495°C | 856°C |
| Sample 5 |  26°C |  1462°C |  1490°C | 784°C |

**Figure 5.** Optical dilatometry results of samples 1 to 5.

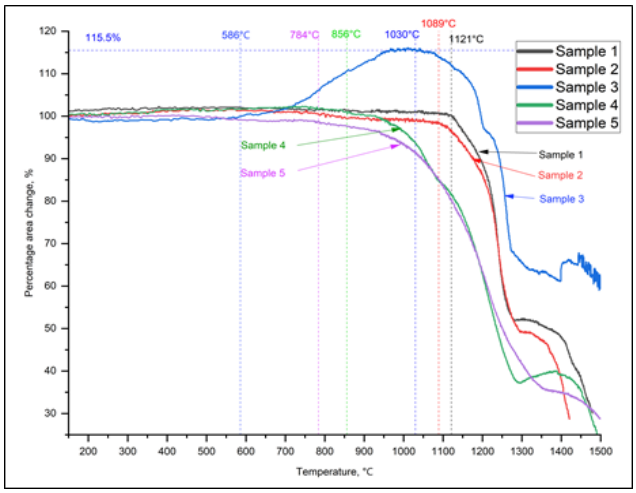



**Figure 6.** Combined dilatometry results, percentage area changes vs. temperature.

and silica) led to decrease in the decomposition temperature of calcite releasing $CO_2$ early[38-40]. Gas release led to a swelling primarily through internal gas pressure that physically pushes particles apart when the gas cannot escape quickly enough. While from 1030°C, it is speculated that due to formation of liquid phases such as calcium ferrite, the area decreased rapidly, or sintering was initiated. Sample 3 exhibited the maximum flow temperature due to higher iron content relative to other samples. Samples 4 and 5 had lower sintering temperature as the carbon starts burning early compared to samples 1 and 2 due to more porous structure of carbon particles[41] illustrated in Figures 4-(a) and (b). Samples 4 and 5 have more amount of LOI % compared to samples 1 and 2, hence

due to evaporation of hydrous vapors, the deformation of test samples commenced at lower temperatures.

Sintering temperature is of great importance for pelletizing and sintering processes as it can decide heat requirements, fuel addition, strength, etc. Minimum sintering temperature helps pellet induration for early slag bonds and better strength[42-44] as well as better melt assimilation and degradation index in sinter making process[45,46] which are both beneficial in iron making processes. Samples 4 and 5 represent the optimal additives for pellet and sinter making considering their favorable sintering temperatures. Furthermore, all samples are viable for these processes as they exhibit sintering temperatures below 1150°C. However, sample 3 exhibited swelling at initial stages, which can be problematic during preheating stage of pelletization and should be carefully managed. However, sample 3 is good source of calcium carbonate which can act like fluxing agent in iron ore pelletizing or sintering process.

## 3.5 Roasting in Bulk TGA

Samples 1 to 5 were pelletized and heat treated in a Bulk TGA furnace at 1300°C, as illustrated in Figure 1

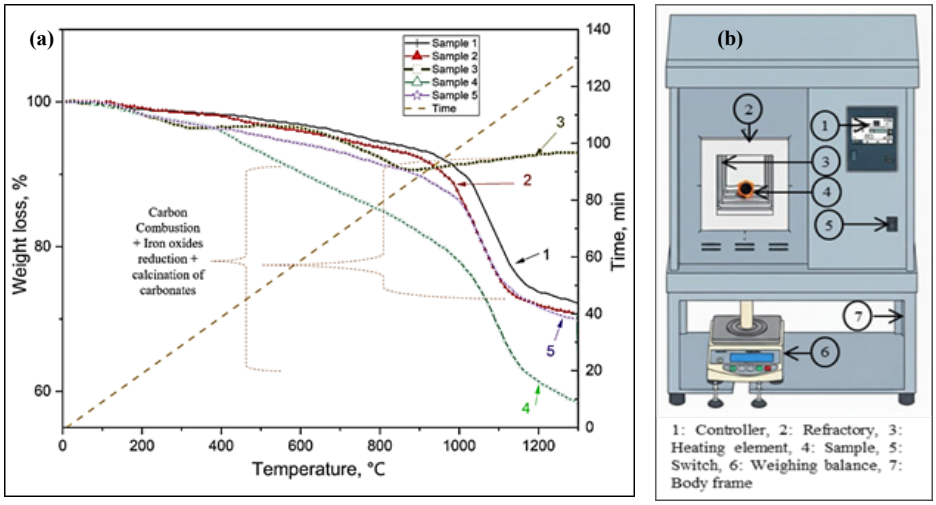



**Figure 7.** **(a)** Bulk TGA graph for 5 samples, Temperature Versus Weight loss and Time. **(b)** Bulk TGA apparatus.

**Table 4.** Chemical analysis of sample 1 to 5 after roasting

| Chemical Composition in % | Sample 1 | Sample 2 | Sample 3 | Sample 4 | Sample 5 |
|---|---|---|---|---|---|
| Total Fe | 44.00 | 44.50 | 52.10 | 41.00 | 42.84 |
| FeO | 24.77 | 24.65 | 3.61 | 23.78 | 7.48 |
| CaO | 6.12 | 6.12 | 15.21 | 5.19 | 7.70 |
| $SiO_2$ | 23.93 | 23.93 | 5.01 | 24.12 | 11.33 |
| MgO | 4.35 | 3.89 | 5.78 | 1.64 | 5.70 |
| $Al_2O_3$ | 5.21 | 5.21 | 1.21 | 4.29 | 4.66 |
| LOI | 0.00 | 0.00 | 0.33 | 0.00 | 0.00 |
| ZnO | 0.11 | 0.47 | 0.56 | 0.14 | 0.11 |

to assess the impact of roasting on composition and zinc phases as well as the variation in weight loss with respect to temperature. Figure 7 depicts mass loss percentage of 5 samples as well as heating profile with respect to temperature. Table 4 presents the chemical analysis of roasted samples.

The thermogravimetric behavior of Samples 1, 2, 4 and 5 shows a progressive decrease in mass consistent with their relatively high carbon content and the reducing conditions generated during heating in air. In both samples, the initial mass loss up to approximately 200 °C corresponds to the evaporation of physically adsorbed moisture. As the temperature increases to 350°C to 700°C, carbon combustion becomes the dominant mechanism of mass reduction, producing $CO_2$ and CO through reactions (1) and (2)[47].

$$C + O_{2(g)} \rightarrow CO_{2(g)} \quad (1)$$

$$2C + O_{2(g)} \rightarrow 2CO_{(g)} \quad (2)$$

The CO produced promotes the reduction of hematite to magnetite, particularly evident in the sharper mass-loss slopes between 600°C and 900°C. These samples also show distinct inflections around 900°C –1100 °C, consistent with the conversion of hematite to lower oxides as per reactions iii, iv and v. The content of zinc oxide after roasting was negligible because the zinc phases were reduced to zinc vapors and evaporated. Although the furnace atmosphere is oxidizing, combustion of carbon within pellets created locally reducing conditions in the pellet interior that promoted the ZnO reduction and Zn volatilization, dominant in samples 4 and 5. After roasting, the condensed zinc vapor formed a residual powder on the crucible rims. This powder was collected and analyzed using SEM-EDS. The nodular microstructure of the pure zinc and zinc oxide is depicted in Figure 4-f. Figure 8 illustrates the zinc content after roasting the raw samples. Samples 1, 2, 4 and 5 exhibited nearly complete reduction of zinc while sample 3 demonstrated minimal zinc reduction attributed to the lower carbon content.

$$3Fe_2O_{3(s)} + CO_{(g)} = 2Fe_3O_4\,(s) + CO_{2(g)} \quad (3)$$

$$Fe3O4_{(s)} + CO_{(g)} = 3FeO_{(s)} + CO_{2(g)} \quad (4)$$

$$FeO_{(s)} + CO_{(g)} = Fe_{(s)} + CO_{2(g)} \quad (5)$$

Sample 4 exhibits the highest overall mass loss among all samples, which corresponds to its larger fraction of carbon and greater CO-induced reduction of iron oxides and zinc oxide, as this is confirmed by XRD studies done after roasting. In contrast, Sample 3 displays a markedly different thermal response because of its very low carbon content and higher iron content. The sample experiences a minor initial mass decrease up to about 600°C associated mainly with moisture and carbon combustion. A more distinct mass loss then occurs between 700°C and 900°C due to carbonate decomposition, represented by reaction (vi).

$$CaCO_{3(s)} \rightarrow CaO + CO_{2(g)} \quad (6)$$

Unlike the carbon-rich samples, which continue to lose mass at high temperature, Sample 3 shows a clear increase in mass between 900°C and 1100°C. This behavior is attributed to the oxidation of lower iron oxides to higher oxides in the oxidizing atmosphere. This oxidation-driven mass gain sharply contrasts with the reduction-dominated behavior of the other samples and directly reflects the limited carbon available to generate reducing conditions. The oxide transformations inferred from these mass-change patterns have been independently confirmed through XRD analysis, which supports the reduction of iron oxides and zinc oxide in the carbon-rich samples and the reverse oxidation sequence in Sample 3 at elevated temperatures.

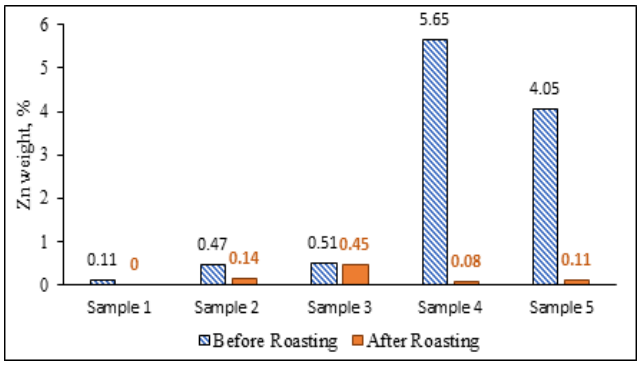



**Figure 8.** Zinc content before and after roasting.

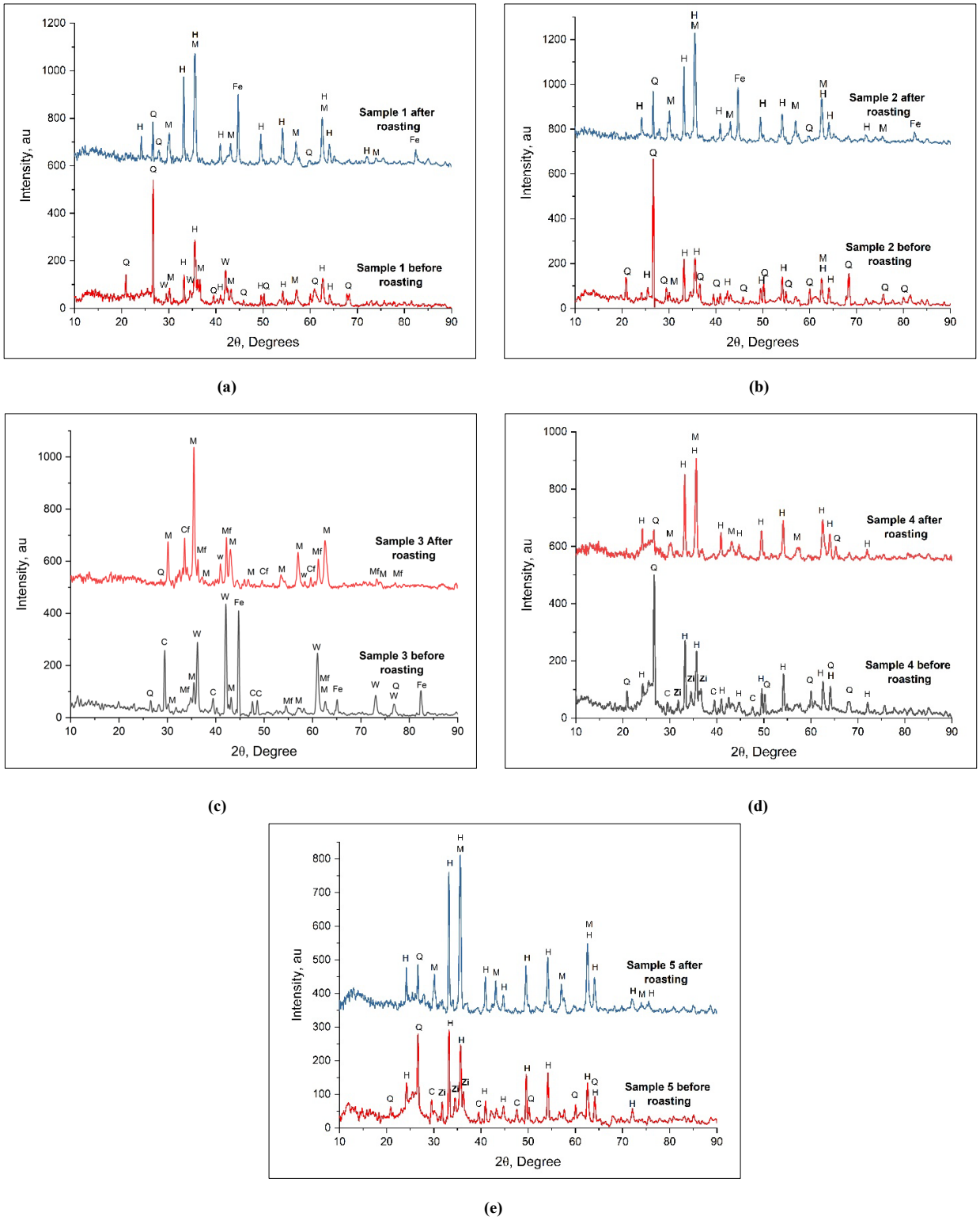



**Figure 9.** Raw Versus roasted samples XRD graphs when heated at temperature at 1300° C, **(a)**-Sample 1, **(b)**-Sample 2, **(c)**-Sample 3, **(d)**-Sample 4, **(e)**-Sample 5. H: Hematite ($Fe_2O_3$), M: Magnetite ($Fe_3O_4$), Q: quartz ($SiO_2$), Zi: Zincite (ZnO), C: Calcite ($CaCO_3$), Cf: Calcium ferrite ($CaFe_2O_4$), Mf: Magnesio ferrite ($MgFe_2O_4$), Fe: metallic iron. W: Wustite (FeO).

### *3.5.1 Phase Analysis after Roasting*

X-Ray Diffraction (XRD) analysis was performed on roasted samples to determine the phases formed. The results, illustrated in Figures 9(a) and 9(b), indicate that both sample 1 and sample 2 after roasting exhibited a mixture of hematite ($Fe_2O_3$), magnetite ($Fe_3O_4$), and metallic iron (Fe). This mixed-phases composition is attributed to the combustion of carbon within the samples. The reducing environment created by the burning carbon facilitated the reduction of some wustite (FeO) and/or magnetite to metallic iron. Importantly, the gangue minerals remained dispersed throughout both sample 1 and sample 2, indicating that the roasting process did not significantly alter their distribution.

In sample 3, Figure 9(c), from the XRD graph it is evident that the roasting process led to a phase transformation of the iron-bearing oxides. Initially, the sample contained wustite (FeO) and metallic iron (Fe). During heating, the mentioned iron phases reacted with preexisting calcite and magnesium oxide (MgO) in the sample yielding calcium ferrite ($CaFe_2O_4$) and magnesioferrite ($MgFe_2O_4$). Any residual unreacted FeO and Fe phases were further oxidized to magnetite ($Fe_3O_4$). The roasting process facilitated a series of reactions resulting in the formation of new iron-containing compounds and higher iron oxides.

Figures 9(d) and 9(e) depicted the XRD graph for roasted samples 4 and 5 respectively, demonstrating the reduction of hematite to magnetite during the roasting process. The presence of minor slag, originating from gangue minerals in the original samples, is identified but could not be confirmed via XRD analysis due to its low concentration or amorphous nature. Importantly, the high degree of zinc volatilization indicates effective reduction of the zinc oxide under the roasting conditions in both samples 4 and 5. This is evidenced by the complete absence of any detectable zinc-containing phases in the post-roasting XRD patterns as well as the chemical analysis after roasting presented in Table 4. According to Ellingham diagram, Figure 10, at temperature 1300°C (1573K), the Gibbs energy versus temperature plotted lines of alumina, silica, magnesium oxide and calcium oxide lie below the zinc oxide line which shows that oxides of Al, Si, Mg and Ca are more stable than zinc oxide[1]. Hence, zinc oxide was reduced before other gangue oxides. While the plotted line in Figure 10 for hematite or magnetite lies above the zinc oxide at temperatures of 1300°C, which shows that iron oxides will be reduced to lower oxide phase before Zinc oxide, due to lower stability.

The Zinc oxide could be reduced by following reactions[48,49]

$$ZnO(s) + C(s) \rightarrow Zn(g) + CO(g),$$
$$\Delta G° = 348480 - (286.1*T) \quad (7)$$

$$ZnO(s) + CO(g) \rightarrow Zn(g) + CO2(g),$$
$$\Delta G° = 178020 - (111.67*T) \quad (8)$$

$$ZnO(s) + Fe \rightarrow Zn(g) + FeO(s),$$
$$\Delta G° = 211089.01 - (143.40*T) \quad (9)$$

According to reaction (vii), by standard Gibbs energy equations, at temperatures above 945°C (1218K), zinc oxide will be reduced by carbon. Also, CO gas produced due to combustion of carbon reduces

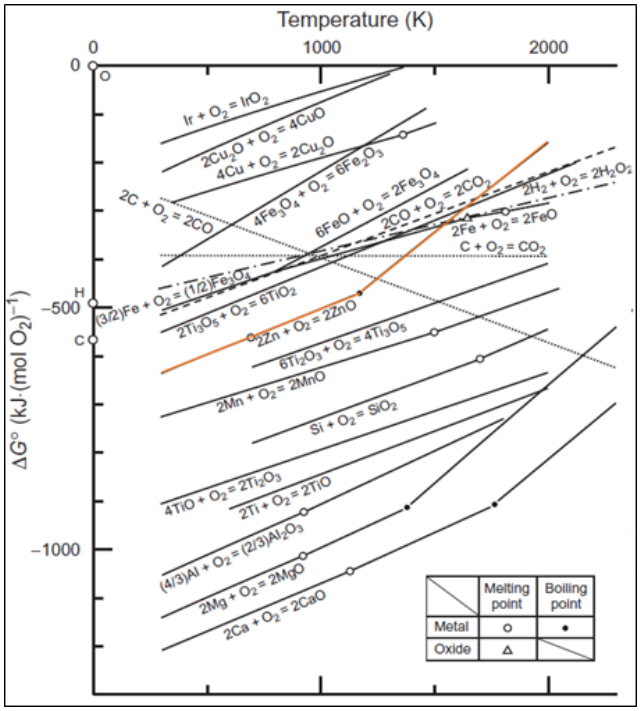



**Figure 10.** Ellingham diagram.

zinc oxide above 1321°C, according to reaction (8). According to reaction (9), above 1200°C, metallic iron reduces zinc oxide. Zinc has boiling point of 907°C, the reaction above this temperature results in vaporization of zinc formed. Since samples 1, 2, 4 and 5 have considerable amounts of carbon, it is most probable that the zinc oxide was reduced by carbon particles and CO gas.

# 4. Discussion

## 4.1 Agglomeration Behavior Inferred from PSD and Microstructure

The particle-size distributions and SEM–EDS observations together indicate that the investigated by-products do not play equivalent roles in agglomeration circuits. Samples 1 and 2, which combine relatively coarse carbonaceous fragments with embedded iron-oxide and gangue grains, are expected to act primarily as fuel-reactive nuclei in sinter beds and as seed particles in green-ball growth, because such composite grains provide mechanical support while supplying localized heat during combustion. In contrast, the finer and more spherical assemblage observed in sample 5 implies better packing and ballability, favoring its use as a high-reactivity fine additive in pellet feeds rather than as a dominant structural component of the burden.

The micro-porous, flocculated texture seen for sample 3 suggests that, without prior conditioning, this material would tend to increase slurry viscosity, water demand and bed resistance in both sinter and pellet plants. However, the same features imply a high specific surface area and ready access of gases, indicating that, once dewatered and micro-pelletized, sample 3 could provide effective fluxed iron units and help fine-tune basicity in the agglomerate. The fluffy ultra-fine clusters and filamentary bridges between carbon and oxide particles in sample 4 point to a stronger tendency to deteriorate permeability than samples 1, 2 and 5, but also to intense reactivity once incorporated in limited amounts, because of the short diffusion paths and intimate solid–solid contacts.

## 4.2 Thermal Performance in Agglomeration Process Inferred from Dilatometry and Bulk TGA

The optical dilatometry results reveal distinct thermal deformation signatures that translate directly into differences in expected burden performance. The relatively low sintering onset temperatures measured for samples 4 and 5 imply that they will contribute to early formation of bonding phases and densification in sinter and pellet beds, enabling target strengths to be achieved at lower peak temperatures or reduced fuel rates compared with feeds relying solely on more refractory ores. In contrast, the higher softening and flow temperatures associated with sample 3 suggest that agglomerates rich in this material will remain mechanically stable deeper into the high-temperature zone, which is beneficial for maintaining bed integrity but may demand higher energy input for complete melt assimilation. The unusual area increases followed by rapid shrinkage observed for sample 3 indicates a propensity for transient swelling during preheating, most plausibly driven by $CO_2$ release from decomposing carbonates and subsequent liquid-phase sintering of newly formed Ca- and Fe-bearing phases. This behavior implies that excessive additions of sample 3 could temporarily reduce bed permeability and disturb gas flow in industrial induration strands, even if the final product strength is acceptable. By comparison, the smoother shrinkage profiles of samples 1, 2, 4 and 5 suggest more gradual densification and fewer risks of abrupt structural changes, supporting their use as additives up to limits dictated primarily by chemistry especially zinc rather than by thermomechanical instability.

## 4.3 Industrial Implementation and Economic Considerations

The integrated flowsheet in Figure 11 provides a practical basis for recycling the five byproducts through both pelletization and sintering process. In the pellet route, only residues finer than about 150μm are suitable, because indurated pellets are highly

sensitive to coarse inclusions and off-spec chemistry. Under these constraints, suitably dezincified fine fractions from samples 4 and 5 can be blended with iron-ore concentrate, fluxes and binder at up to about 2 wt.%, preserving pellet strength and reducibility while partial substitution of solid fuel. Coarser or highly fluffy fractions are instead directed to the sinter route, where raw materials are typically below 10 mm, but excessive ultra-fines would impair bed permeability and flame-front stability[9,31].

Samples 1 and 2 characterized by moderate Fe, significant fixed carbon and low Zn—can be charged directly to the base mix, taking advantage of the broader PSD tolerance of sinter plants and the fact that their zinc levels remain below those that usually trigger problematic zinc recirculation in the blast furnace. In this role they function as fuel-reactive nuclei and secondary iron units, reducing demand for coke breeze and ore fines. Sample 3, richer in Fe and CaO, behaves as a combined iron–flux source; plant and laboratory studies have shown that sludges can be incorporated into sinter feeds at controlled rates without detrimental effects on strength or basic indices, while partially replacing limestone and ore in the burden. Samples 4 and 5, by contrast, require prior dezincification because their high ZnO content and ultrafine, fluffy morphology would otherwise aggravate zinc buildup and degrade bed permeability. Pyrometallurgical treatment in a Rotary Hearth Furnace (RHF) is particularly suitable: industrial RHF operations routinely achieve dezincing ratios around 80–90 % with metallization of 70–80 %, producing a low-Zn DRI product that can be returned to the blast furnace or steel making and a ZnO-rich secondary dust suitable for sale or further refining. After RHF treatment, the fine DRI fraction derived from samples 4 and 5 can be managed in the same way as samples 1–3, ensuring that zinc is removed from internal circulation while retaining iron value[19,50-52].

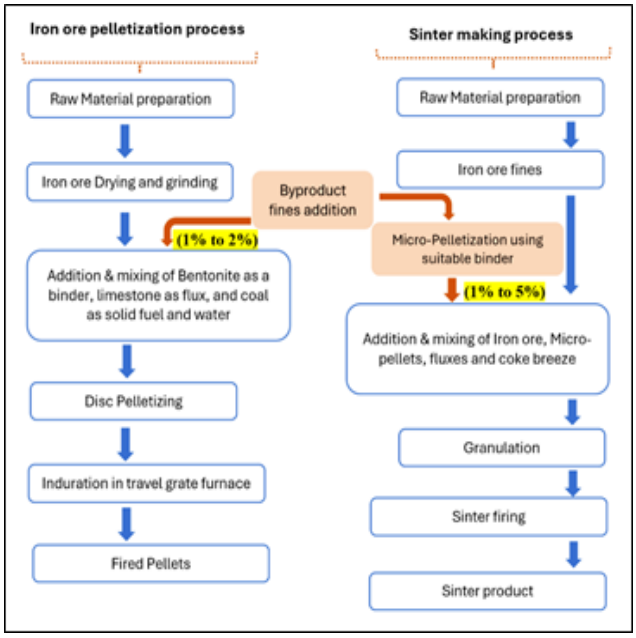



**Figure 11.** Schematic process flow for iron ore pelletization and sintering process in which by-products are incorporated in the respective stages.

To restore permeability and handling characteristics in the sinter bed, by-products (samples 1–3) together with dezincified fines from samples 4 and 5 should be first micro-pelletized into 1–6 mm granules using a process-friendly binder. Industrial micro-pelletization trials with mixed steel-plant sludges and dusts report that additions of roughly 1–5 wt.% micro-pellets in the sinter base mix can be accommodated without compromising sinter strength, productivity or reducibility, while recycling tens of kilograms of waste per ton of sinter. Economically, this integrated strategy is attractive because by-products displace higher-value iron ore, coke breeze and flux, while reducing the liabilities associated with storage and external disposal of dusts and sludges[51,53-55]. RHF treatment of high-zinc residues adds a revenue stream through saleable ZnO fume and low-Zn DRI, and micro-pelletization converts otherwise land-locked ultra-fine wastes into process-friendly feed, offering a realistic pathway towards near-zero-waste operation in integrated steelworks.

## 5. Conclusion

This study systematically evaluated zinc-bearing by-products from an integrated steel plant to assess their suitability for sustainable recycling through agglomeration processes. Comprehensive characterization using particle size analysis, SEM–

EDS, XRD, dilatometry and Bulk TGA revealed strong correlations between morphology, phase assemblage, and high-temperature behavior.

Particle size and XRD analyses confirmed clear compositional differences among the five samples. Samples 1 and 2 showed coarser distributions dominated by hematite, magnetite, and silica, while Samples 4 and 5 contained finer particles enriched with zincite. Sample 3 exhibited a broader distribution with significant calcite and wustite. These variations governed their distinct thermal and zinc-bearing behavior.

Microstructure and dilatometry revealed that Samples 1 and 2 possess compact carbon–oxide matrices favorable for sintering and pelletizing, whereas Samples 4 and 5 exhibit ultrafine, porous assemblages that promote early sintering at lower temperatures. Sample 3 showed swelling linked to calcite breakdown, indicating more restrictive use in agglomeration. Overall, Samples 4 and 5 are the most thermally suited for agglomeration processes.

Bulk TGA showed strong mass loss in Samples 1, 2, 4, and 5 due to carbon combustion and CO-driven iron-oxide reduction, enabling efficient zinc volatilization at 1300°C. Sample 3, with low carbon, exhibited limited reduction and instead showed carbonate decomposition followed by high-temperature oxidation.

Post-roasting XRD confirmed reduction pathways in Samples 1, 2, 4, and 5 (hematite → magnetite → FeO) alongside near-complete zinc removal. Sample 3 transformed oxidatively to calcium ferrite, magnesioferrite, and higher iron oxides, retaining most of its zinc. These phase evolutions validate the distinct reductive and oxidative behaviors observed in TGA.

## 6. Compliance with Ethical Standards

Conflict of Interest: On behalf of all authors, the corresponding author states that there is no conflict of interest.

## 7. Funding

This work was supported by Tata Steel Ltd, Jamshedpur.

## 8. Acknowledgements

The author would like to express sincere gratitude to Tata Steel R&D for their invaluable support and resources throughout the course of this research. The author also wishes to extend appreciation to the supporting staff and colleagues, whose assistance and insights were instrumental in navigating various challenges during the research process.

## 9. References

1. Seshadri S, Hasegawa M. Ellingham diagram. In: Treatise on Process Metallurgy. Elsevier; 2014. p. 507-510. https://doi.org/10.1016/B978-0-08-096986-2.00032-1 PMCid:PMC4371565
2. Jikar PC, Dhokey NB. Overview on production of reduced iron powder from mill scale waste. Mater Today Proc. 2021; 44:4324-4329. https://doi.org/10.1016/j.matpr.2020.10.552
3. Indian Bureau of Mines. Indian Minerals Yearbook 2018 (Part II: Metals and Alloys). Nagpur: IBM; 2018.
4. Jinyu Z, Zihan L, Qiang G. Comprehensive utilisation of blast furnace slag. Can Metall Q. 2024; 63(3):927-934. https://doi.org/10.1080/00084433.2023.2235147
5. Hsing JH, Atsushi I. Chemical-free pressure-swing carbonation of blast furnace slag for $CO_2$ utilization and sequestration. ACS Sustain Chem Eng. 2025; 10:3842-3852. https://doi.org/10.1021/acssuschemeng.4c05872
6. Mamdouh O, Fabritius T, Paananen T. Effect of blast furnace sludge characteristics on suitable recycling process. J Miner Mater Charact Eng. 2017; 5:185-197. https://doi.org/10.4236/jmmce.2017.54016
7. Khokhar S, Goyal V, Kumar N, Usha K, Pandey V, Sharma J, *et al.,* Enriched LD slag application for improving grain yield and quality of wheat. J Environ Biol. 2024; 45(6):666-675. https://doi.org/10.22438/jeb/45/6/MRN-5374
8. Swarnakar A, Biswas C, Majumdar A, Dey R. Utilization of steel plant wastes to produce metallic iron. J Inst

Eng India Ser D. 2023; 105:1251-1259. https://doi.org/10.1007/s40033-023-00502-w

9. Das B, Prakash S, Reddy PSR, Misra VN. Utilization of slag and sludge from steel industries. Resour Conserv Recycl. 2007; 50(1):40-57. https://doi.org/10.1016/j.resconrec.2006.05.008
10. Umadevi T, Kumar SMG, Mahapatra PC, Babu MT. Recycling of steel plant mill scale via pelletisation. Ironmak Steelmak. 2009; 36(6):409-415. https://doi.org/10.1179/174328108X393795
11. Gaballah NM, Zikry AF, Khalifa MG, Farag AB, El-Hussiny NA, Shalabi MEH. Production of iron from mill scale waste via hydrogen. Open J Inorg Non-Met Mater.2013; 3:23-28. https://doi.org/10.4236/ojinm.2013.33005
12. Zhao Y, Chan WP, Chin V, Boon YZ, Fu X, Gu Y, *et al.,* Environmental assessment of sludge-derived slag. Waste Manag. 2024; 190:186-196. https://doi.org/10.1016/j.wasman.2024.09.021 PMid:39332347.
13. Trinkel V, Mallow O, Aschenbrenner P, Rechberger H, Fellner J. Characterization of blast furnace sludge. Ind Eng Chem Res. 2016; 55:5590-5597. https://doi.org/10.1021/acs.iecr.6b00617
14. Dutta SK. Utilization of iron ore fines and steel plant wastes. JPC Bull. 2019; 25-33.
15. Greenco Sustainable usage of LD waste. 2023; https://www.greenco.in/ciienv/endoc23/Tata%20Steel.pdf
16. Jena MK, Mahanta J, Mahapatra MM, Baliarsingh M, Mishra S. Recovery of iron from blast furnace sludge. In: Lecture Notes in Mechanical Engineering. Singapore; 2023.
17. Mend B, Lee YJ, Kwon DY, Bang JH, Chu YS. Sludge-derived ferrous sulfate use in cement. Adv Cem Res. 2025;1-9.
18. Sayaf M, Liqun L, Bo-Tao Z, Chen XW, Niyonzima C. Lead and zinc impurities in ironmaking. Metals. 2021; 11:407-426. https://doi.org/10.3390/met11030407
19. Pal J, Ghorai S, Venkatesh P, Goswami M, Bandyopadhyay D. Fluxed micropellets using iron waste. Ironmak Steelmak. 2013; 40:498-505. https://doi.org/10.1179/1743281212Y.0000000069
20. Sharanappa K, Ratnakar B, Rudramuniyappa M, Singh L. HMDS vs LD slag in sinter making. Int J Creat Res Thoughts. 2018; 68-77.
21. Mogale A, Das S, Mrigandra S, Vijay C, Sujoy H. Iron ore pellets with mill scale. J Sustain Metall. 2024; 10:2311-2324. https://doi.org/10.1007/s40831-024-00918-y
22. Prasad D, Kumari R, Arunkumar CA, Sankar B, Sinha S. Micro pelletizing innovations. Eng Headway. 2025; 22:39-44. https://doi.org/10.4028/p-Xz6TKy
23. Besta P, Janovska K, Samolejova A, Bernkova A, Voznakova I, Hendrych M. Zinc cycle in blast furnace. Metalurgija. 2013; 197-200.
24. Dastidar M, Sarkar B, Mitra M, Dey R. Alkali effects in ironmaking. Mater Sci Eng Int J. 2018; 6:304-313.
25. Besta P, Sikorova A, Kubica S, Vilamova S, Prosicky P. Zinc compounds impact on furnace lining. In: METAL 2015; Brno.
26. Guanbo W, Yanling Z, Guoguang C, Zhongzhong X, Changfu D, Long H. Zn oxide behavior in pellets. J Mater Res Technol. 2023; 7583-7593.
27. Xie Z, Jiang T, Guo Y, Wang S, Chen F, Yang L. Zinc separation by roasting and leaching. Separations.2023; 10:299-312. https://doi.org/10.3390/separations10050299
28. Nabeel M. Study of microparticles in ironmaking. Stockholm: KTH Royal Institute of Technology; 2016.
29. Ciocan A, Potecasu F, Ivamcea L. Dust particle morphology in blast furnace gas. Ann Univ Galati Metall Mater Sci. 2009; (2):95-100.
30. Rout K. Characterization of iron ore pellet agglomerates. Int J Creat Res Thoughts. 2018; 6(1):1009-1019.
31. Navaei S, Ghorbani M, Sheibani S, Hosseini L, Zare M. A review on hematite concentrate pelletization: effect of process parameters on iron ore pellet quality. J Mater Res Technol. 2025; 38:4849-4859. https://doi.org/10.1016/j.jmrt.2025.08.295
32. Li Z, Zhang J, Wang Y, Lu L, Jiang H, Tan Y, *et al.,* Pellet consolidation strength improvement. Steel Res Int. 2022; 93(10):2200084. https://doi.org/10.1002/srin.202200084
33. Lau LL, Strezov V, Gonçalves MVB, Bagatini MC. Trace elements in sintering. Environ Adv. 2021; 6:100123. https://doi.org/10.1016/j.envadv.2021.100123
34. Su F, Lampinen HO, Robinson R. Recycling sludge to BOF converter. ISIJ Int. 2004; 44(4):770-776. https://doi.org/10.2355/isijinternational.44.770
35. Swain PK, Biswal T, Kar PK, Panda RB. Waste recycling in steel plant. J Ind Pollut Control. 2017.
36. Singh PK, Katiyar P, Kumar AL, Chaithnya B, Pramanik S. Blast furnace waste pellets. Procedia Mater Sci. 2014.

37. Mombelli D, Cecca CD, Mapelli C, Barella S, Bondi E. BF sludge uses in DRI production. Process Saf Environ Prot. 2016; 102:410-420. https://doi.org/10.1016/j.psep.2016.04.017

38. Lu H, Li CX, Mao WW, Li H. $CaCO_3$ decomposition study. Metall Res Technol. 2017; 114:119. https://doi.org/10.1051/metal/2016070

39. Dai-xi L, Hong-yun S, Jie D, Yuan-zhi X. Thermal decomposition kinetics of $CaCO_3$. Chem Biotechnol. 2003; 4:363-368. https://doi.org/10.1631/jzus.2003.0363 PMid:12765294.

40. Baudin F, Bouton N, Wattripont A, Carrier X. Carbonate decomposition kinetics. Sci Technol Energy Transit. 2023; 78(38):1-13. https://doi.org/10.2516/stet/2023038

41. Zhang Y, Xueqing Z, Wen Y, Haihui X, Sherong H, Song Y. Coal combustion pore structure. Sci Rep. 2020; 10:7125.

42. Liu ZJ, Ma LM, Zhang JL, Wang YZ, Cai QY, Jiang HQ, *et al.,* Slag formation in pellets. Calphad. 2024; 87:102729. https://doi.org/10.1016/j.calphad.2024.102729

43. Liu K, Chen F, Guo Y, Liu Y, Wang S, Yang L. Basicity impact on pellets. Metals. 2022; 12:1057. https://doi.org/10.3390/met12061057

44. Basha SM, Dwarapudi S, Basaveswara RP, Indrajit P, Sinha S, Tudu S. $CO_2$-free flux for pelletizing. Min Metall Explor. 2024; 41:1035-1050. https://doi.org/10.1007/s42461-024-00949-9

45. Kumar S, Jaiswal A, Sah R. Improving sinter productivity. J Min Metall B. 2022; 58(2):261-273. https://doi.org/10.2298/JMMB210922009K

46. Rajak DK, Agrawal S, Dwarapudi S, Paswan RK, Sinha SK, Banerjee D, *et al.,* Increasing sinter productivity using permeability bars. Ironmak Steelmak. 2025. https://doi.org/10.1177/03019233241292383

47. Mamdouh O, Fabritius T, Yaowei Y, Guo C. Analysis of BF and BOF sludge behavior. Metals. 2020; 10:397-407. https://doi.org/10.3390/met10030397

48. Xiaolong L, Zhiwei P, Jiaxing Y. Recycling electric arc furnace dust. J Clean Prod. 2017; 149:1079-1100. https://doi.org/10.1016/j.jclepro.2017.02.128

49. Sung MJ, Hyung SK, Ji-Whan A, Kim H. Zn recovery from EAF dust. In: East Asian Recycling Technology Symposium; 2001; 23-25.

50. Furukawa T, *et al.,* Dust and sludge recycling with the rotary hearth furnace. Nippon Steel Tech Rep. 2005; (92):88-92.

51. Xue Y, Hao X, Liu X, Zhang N. Recovery of zinc and iron from steel mill dust: an overview of available technologies. Materials (Basel). 2022; 15(12):4127. https://doi.org/10.3390/ma15124127 PMid:35744185 PMCid:PMC9228750.

52. Rout K, Mohanty B, Pattanayak SK. Characterisation and reuse avenues of blast furnace sludge (solid metallurgical waste) and recycling of sludge pond effluents. Int J Innov Sci Res Technol.2018; 3(1):462-470.

53. Sun H, Li J, Zhang Y, *et al.,* Development of fluxed micropellets for sintering utilising iron oxide waste fines. Ironmak Steelmak. 2014; 41(1):55-61.

54. Stewart DJ, Scrimshire A, Thomson D, Bingham PA, Barron AR. The chemical suitability for recycling of zinc contaminated steelmaking by-product dusts: the case of the UK steel plant. Resour Conserv Recycl Adv. 2022; 14:200073. https://doi.org/10.1016/j.rcradv.2022.200073

55. Das P, Upadhyay S, Dubey S, Singh KK. Waste to wealth: recovery of value-added products from steel slag. J Environ Chem Eng. 2021; 9(5):105640 https://doi.org/10.1016/j.jece.2021.105640

## Author Contribution

Khedkar Vinayak Jivanrao: Conceptualization, Methodology, Formal analysis, Investigation, Writing - Original draft preparation, Writing- Review and editing; Shaikh Mahaboob Basha: Writing- Review and editing; Munukutla Sri Sai Ramesh: Writing- Review and editing; Srinivas Dwarapudi: Writing- Review and Editing, Atanu Ranjan Pal: Resources, Review and Editing, Supervision.